CASE 1: TIME-ACCURATE NUMERICAL SIMULATIONS OF SYNTHETIC JETS IN QUIESCENT AIR

K-A. B. Rupesh[1], B. R. Ravi[1], R. Mittal[1], R. Raju[1], Q. Gallas[2], and L. Cattafesta[2]

[1]*Department of Mechanical & Aerospace Engineering,*
The George Washington University, Washington, DC 20052.
[2]*Department of Mechanical & Aerospace Engineering,*
University of Florida, Gainesville, FL 32611.

Introduction

The unsteady evolution of three-dimensional synthetic jet into quiescent air is studied by time-accurate numerical simulations using a second-order accurate mixed explicit-implicit fractional step scheme on Cartesian grids. Both two-dimensional and three-dimensional calculations of synthetic jet are carried out at a Reynolds number (based on average velocity during the discharge phase of the cycle $V_{j,}$ and jet width d) of 750 and Stokes number of 17.02. The results obtained are assessed against PIV and hotwire measurements provided for the NASA LaRC workshop on CFD validation of synthetic jets.

Numerical Methodology

The evolution of zero-net mass-flux synthetic jet from a cavity into quiescent air is modeled by the unsteady, incompressible Navier-Stokes equations, written in tensor form as

$$\frac{\partial u_i}{\partial x_i}=0; \quad \frac{\partial u_i}{\partial t}+\frac{\partial u_i u_j}{\partial x_j}=-\frac{\partial p}{\partial x_i}+\frac{1}{\mathrm{Re}}\frac{\partial^2 u_i}{\partial x_j \partial x_j}$$

where the indices, $i = 1, 2, 3,$ represent the x, y and z directions, respectively; while the velocity components are denoted by u (u_1), v (u_2) and w (u_3), respectively. The equations are nondimensionalized with the appropriate length and velocity scales where *Re* represents the Reynolds number. The Navier-Stokes equations are discretized using a cell-centered, collocated (non-staggered) arrangement of the primitive variables ($\vec{u}$, p). In addition to the cell-center velocities ($\vec{u}$), the face-center velocities, $\vec{U}$, are also computed. Similar to a fully staggered arrangement, only the component normal to the cell-face is calculated and stored. The face-center velocity is used for computing the volume flux from each cell. The advantage of separately computing the face-center velocities has been discussed in the context of the current method in Ye *et al.* [1]. The equations are integrated in time using the fractional step method. In the first step, the momentum equations without the pressure gradient terms are first advanced in time. In the second step, the pressure field is computed by solving a Poisson equation. A second-order Adams-Bashforth scheme is employed for the convective terms while the diffusion terms are discretized using an implicit Crank-Nicolson scheme which eliminates the viscous stability constraint. The pressure Poisson equation is solved with a Krylov-based approach.

The solver uses a multi-dimensional ghost-cell methodology to incorporate the effect of the immersed boundary on the flow; however, the absence of curvilinear topology in the geometry makes this approach unnecessary in the current study. Care has been taken to ensure that the discretized equations satisfy local and global mass conservation constraints as well as pressure-velocity compatibility relations. The code has been rigorously validated by comparisons against established experimental and computational data. Details have been presented elsewhere [2, 3].

Implementation and Case Specific Details

The present study models the flow inside the cavity using a pulsatile velocity boundary condition, $v = v_o \sin(\omega t)$ prescribed at the bottom of the cavity (see Fig. 1) in order to generate a natural flow at the slot exit. The shape of the cavity is approximated to be a rectangular box without taking into consideration the finer details that make up the interior of the cavity. However, the geometrical and flow parameters used in the current study are chosen based on a scaling analysis of various parameters involved like slot width *(d)*, slot height *(h)*, cavity width *(W),* cavity height *(H),* the diaphragm vibrating frequency *(f),* etc.. For instance, the slot size is chosen such that the ratio *h/d* and *W/d* match those used in the experiments; however, *H/d* of 4.95 used in the calculations is not matched in the experiments. The Reynolds number (Re) in this work is defined based on average jet velocity during the discharge phase of the cycle *(V_j)* and jet width (d) i.e., $\mathrm{Re} = V_j d / \upsilon$. Average jet velocity *(V_j)* in the numerical calculations is set equal to the value of 10.5 *m/s,* obtained by averaging the velocity provided by the LDV measurements during the discharge phase of the cycle. Because of the uncertainty in V_j reported by different measurements, a nominal Re of 750 corresponding to the lower bound of V_j calculated from the measurements is chosen in the present investigation. Experimental values of ω = 2794 *rad/s, d* = 1.27 *mm and* υ = 1.5527x10^{-5} m^2/s are matched to give a Stokes number ($S = \sqrt{\omega d^2 / \upsilon}$) of 17.02 in the computations. Various cases considered in the present study and the corresponding flow parameters are detailed in Table 1.

#	*Re*	2D/3D	*S*	Exterior Domain Size	Grid Size	Time steps/cycle N	$\Delta t = \dfrac{2\pi}{\omega N}$
1.	750	3D	17.02	30dx 30d x 3d	132x250x 16	14,000	0.00116144
2.	750	2D	17.02	30d x 30d	132 x 220	14,000	0.00116144

Table 1.Various cases considered in the study and their flow parameters.

Figure 1 shows the schematic of the computational domain and the boundary conditions used in the computations. An outflow velocity boundary condition is prescribed at the left, right and top boundaries that allow them to respond freely to the flow created by the jet. In 3D calculations, periodic boundary conditions are prescribed in the span wise *(z)* direction. Figure 2 shows an *x-y* slice of a typical 3D mesh used in the region near the slot in the computations. Grids used in the current work are non-uniform in both *x-* and *y-* directions, and uniform in the span wise *(z)* direction in the case of 3D calculations.

Sufficient clustering is provided in the slot-region along *x*- and *y*-directions to resolve the vortex structures that form at the slot exit, as well as the shear layer in the slot. Typically 32 grid points clustered using a cosine-hyperbolic distribution are used across the slot. In 3D calculations, the three-dimensionality in the solution is instigated by introducing a small sinusoidal spatial perturbation in the z-component of velocity *(w)* over a few hundred time-steps in the first cycle. For all cases presented here, the first two cycles of calculations are not included in the averaging process to eliminate transient effects, and the next two to three cycles are used in the process.

Results

Figure 3 shows the isosurfaces of vorticity magnitude obtained from three-dimensional calculation before the onset of full three-dimensionality in the solution. It is clear from the figure that the flow is dominated by counter-rotating vortex pairs. Figure 4 shows the isosurfaces of vorticity magnitude for the same solution after the onset of full three-dimensionality. Figure 4 shows two pairs of rib vortices along the span obtained from the 3D simulation. The plot of phase-averaged *v*-velocity component vs. phase angle ϕ at the point (*x, y*) = (0 *mm,* 0.1 *mm*) shown in Figure 5 describes the procedure involved in aligning the CFD data with PIV data. Phase angle at which $V_{avg} = (V_{max+} V_{min})/2$ intersects the curve is made 340^{o} by applying the required phase shift. Figure 6 shows the plot of phase-averaged *v*-velocity component vs. phase angle ϕ at the point (*x, y*) = (*0 mm, 0.1 mm*) for the two calculations and it can be seen that the CFD data is reasonably aligned with the PIV data. Plot of time-averaged *u*- and *v*-velocity components at the point (*x, y*) = (*0 mm, 0.1 mm*) across the slot region is shown in Figure 7. Figure 8 and 9 show the comparison of phase-averaged *u*- and *v*-velocity components at the same point at $\phi = 90^{o}$ and $\phi = 270^{o}$ respectively. Three-dimensional calculations at Re > 1000 corresponding to the upper bound of V_j reported in the experiments are being carried out and since the solutions at these Reynolds numbers were not converged at the time of preparation of this report, they would be presented in detail at the workshop.

Acknowledgements

This work is supported by NASA (Grant NAG-1-01024) and AFOSR (Grant F49620-03-1-0146 and F49620-03-1-0135).

References

[1] Ye, T., Mittal, R., Udaykumar, H. S. and Shyy, W., "An Accurate Cartesian Grid Method for Viscous Incompressible Flows with Complex Immersed Boundaries," *J. Comp. Phys.* Vol. 156, pp. 209-240, 1999.

[2] Ravi, B. R., Mittal, R., and Najjar, F. M., "Study of Three-Dimensional Synthetic jet Flowfields Using Direct Numerical Simulation," *AIAA 2004-0091,* 2004.

[3] Najjar, F.M., and Mittal, R., "Simulations of Complex Flows and Fluid-Structure Interaction Problems on Fixed Cartesian Grids," *FEDSM 2003-45577*, Proceedings of FEDSM'03, 4th ASME-JSME Joint Fluids Engineering Conference, July 6-11, Honolulu, Hawaii, 2003

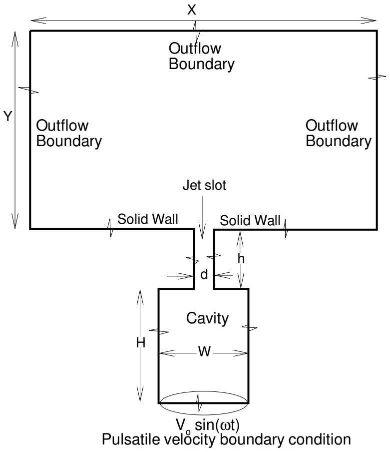

Figure 1: Schematic of the computational domain and boundary conditions.

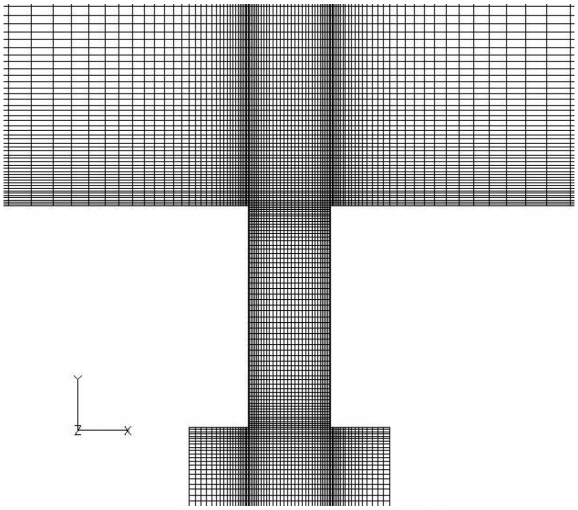

Figure 2: A typical grid in the slot region used in the computations.

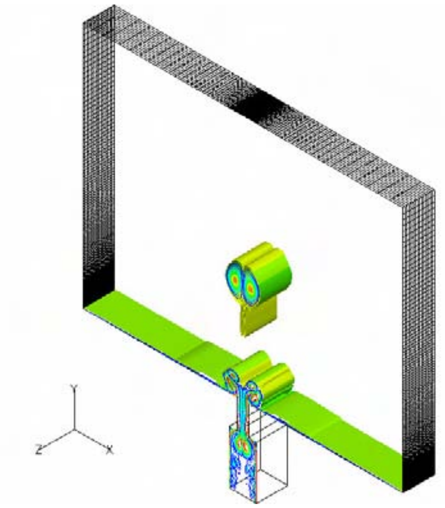

Figure 3: Isosurfaces of vorticity magnitude 2^{nd} cycle, Re = 750, S = 17.02.

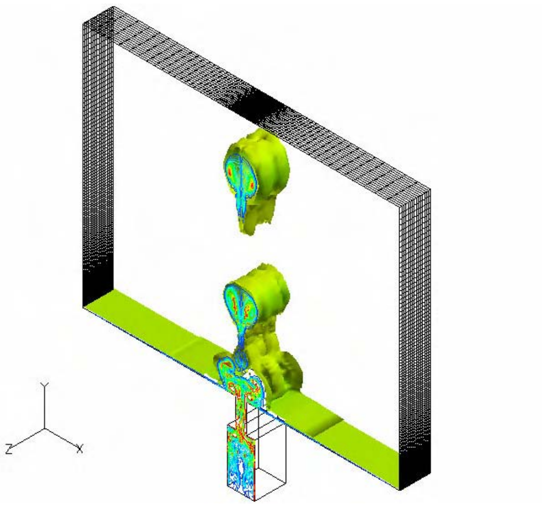

Figure 4: Isosurfaces of vorticity magnitude 3^{rd} cycle, Re = 750, S = 17.02

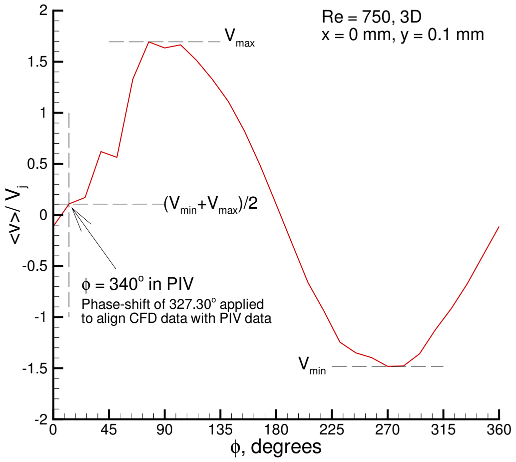

Figure 5: Plot of phase-averaged v vs. phase angle before aligning CFD data with PIV data.

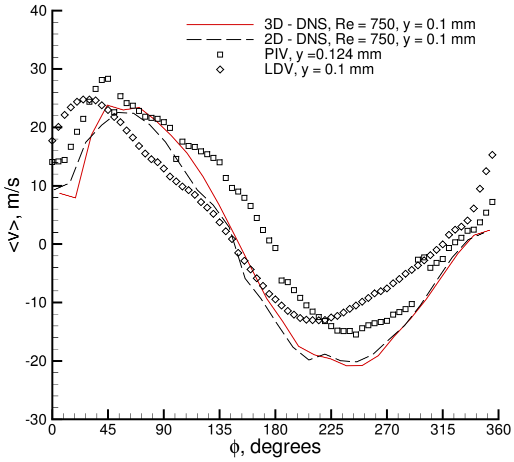

Figure 6: Plot of phase-averaged v vs. phase angle after aligning CFD data with PIV data.

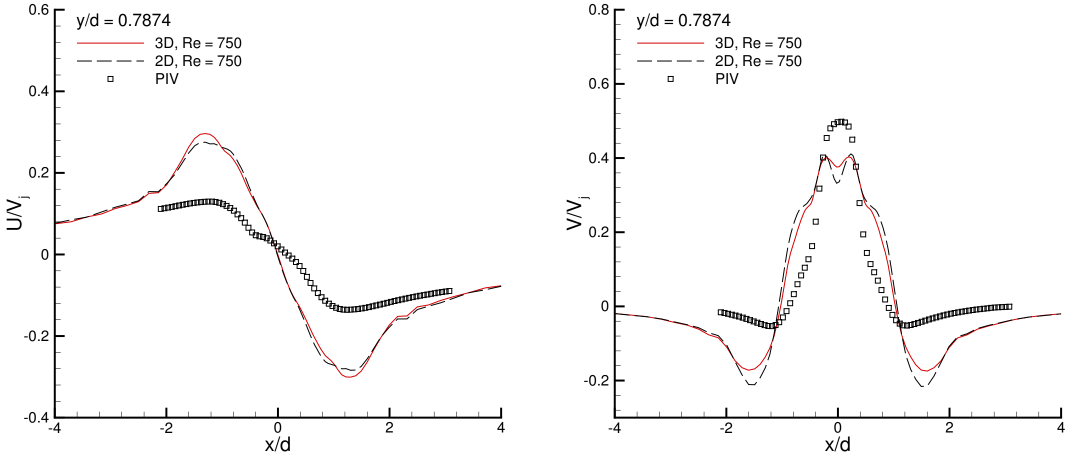

Figure 7: Plot of time-averaged u- and v-velocities along the horizontal line y = 0.7874 (≈1mm in the experiments).

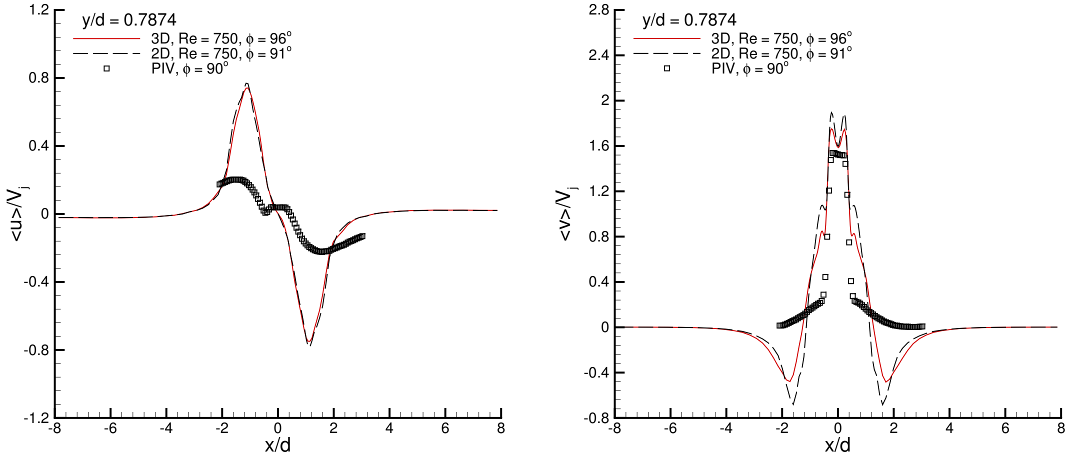

Figure 8: Plot of phase-averaged u- and v-velocities along the horizontal line y = 0.7874 (≈1mm in the experiments) at $\phi = 90^{\mathrm{o}}$ degrees.

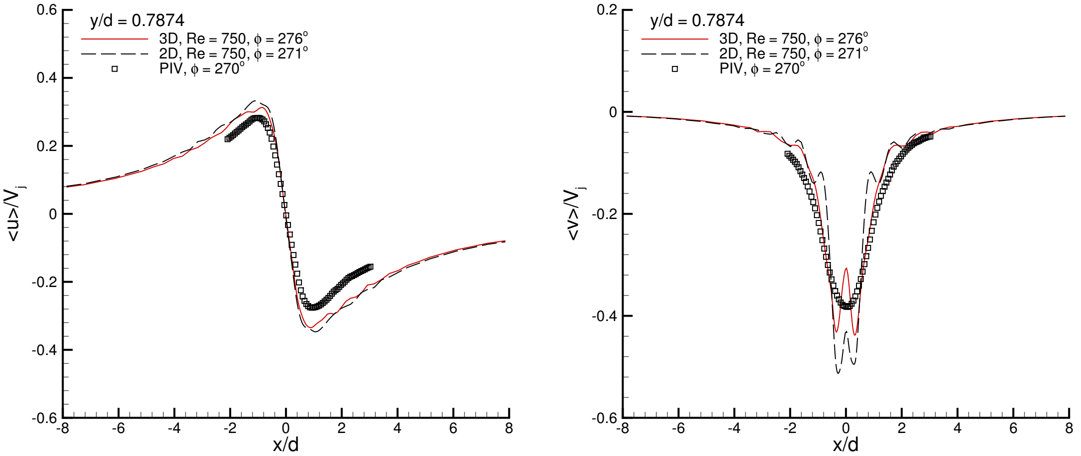

Figure 9: Plot of phase-averaged u- and v-velocities along the horizontal line y = 0.7874 (≈1mm in the experiments) at $\phi = 270^{\mathrm{o}}$ degrees.